Early calcium handling imbalance in pressure overload-induced heart failure with nearly normal left ventricular ejection fraction

Sarah Rouhana, Charlotte Farah, Jérôme Roy, Amanda Finan, Glaucy Rodrigues de Araujo, Patrice Bideaux, Valérie Scheuermann, Youakim Saliba, Cyril Reboul, Olivier Cazorla, et al.

To cite this version:

Sarah Rouhana, Charlotte Farah, Jérôme Roy, Amanda Finan, Glaucy Rodrigues de Araujo, et al.. Early calcium handling imbalance in pressure overload-induced heart failure with nearly normal left ventricular ejection fraction. Biochimica et Biophysica Acta - Molecular Basis of Disease, 2019, 1865 (1), pp.230-242. ⟨10.1016/j.bbadis.2018.08.005⟩. ⟨hal-01856045⟩

HAL Id: hal-01856045
https://hal.umontpellier.fr/hal-01856045v1

Submitted on 22 Jan 2020

Early calcium handling imbalance in pressure overload-induced heart failure with nearly normal left ventricular ejection fraction

Sarah Rouhana[a,b,1], Charlotte Farah[a,1], Jerome Roy[a], Amanda Finan[a], Glaucy Rodrigues de Araujo[a,c], Patrice Bideaux[a], Valérie Scheuermann[a], Youakim Saliba[b], Cyril Reboul[d], Olivier Cazorla[a], Franck Aimond[a], Sylvain Richard[a,*], Jérôme Thireau[a], Nassim Fares[b]

[a] PhyMedExp, Université de Montpellier, INSERM, CNRS, France
[b] Université Saint Joseph, Beyrouth, Lebanon
[c] CiPharma, Escola de Farmácia, Universidade Federal de Ouro Preto, Minas Gerais, Brazil
[d] Université Avignon, LAPEC EA4278, Avignon, France

Keywords:
Heart failure with preserved ejection fraction
Hypertension
Cardiomyocytes
Calcium

ABSTRACT

Heart failure with preserved ejection fraction (HFpEF) is a common clinical syndrome associated with high morbidity and mortality. Therapeutic options are limited due to a lack of knowledge of the pathology and its evolution. We investigated the cellular phenotype and Ca^{2+} handling in hearts recapitulating HFpEF criteria. HFpEF was induced in a portion of male *Wistar* rats four weeks after abdominal aortic banding. These animals had nearly normal ejection fraction and presented elevated blood pressure, lung congestion, concentric hypertrophy, increased LV mass, wall stiffness, impaired active relaxation and passive filling of the left ventricle, enlarged left atrium, and cardiomyocyte hypertrophy. Left ventricular cell contraction was stronger and the Ca^{2+} transient larger. Ca^{2+} cycling was modified with a RyR2 mediated Ca^{2+} leak from the sarcoplasmic reticulum and impaired Ca^{2+} extrusion through the Sodium/Calcium exchanger (NCX), which promoted an increase in diastolic Ca^{2+}. The Sarcoplasmic/endoplasmic reticulum Ca^{2+} ATPase (SERCA2a) and NCX protein levels were unchanged. The phospholamban (PLN) to SERCA2a ratio was augmented in favor of an inhibitory effect on the SERCA2a activity. Conversely, PLN phosphorylation at the calmodulin-dependent kinase II (CaMKII)-specific site (PLN-Thr17), which promotes SERCA2A activity, was increased as well, suggesting an adaptive compensation of Ca^{2+} cycling. Altogether our findings show that cardiac remodeling in hearts with a HFpEF status differs from that known for heart failure with reduced ejection fraction. These data also underscore the interdependence between systolic and diastolic "adaptations" of Ca^{2+} cycling with complex compensative interactions between Ca^{2+} handling partner and regulatory proteins.

1. Introduction

Heart failure (HF) has historically been defined by the inability of the myocardium to pump blood normally due to an impaired systolic contractile performance of the left ventricle (LV). Recently, cardiologists have identified a subtype of HF presenting clinical signs and symptoms of HF but with normal or nearly normal left ventricular ejection fraction (LVEF) [1–4]. In fact, half of all patients with HF are classified as having diastolic dysfunction and a relatively preserved EF (HFpEF). The diagnosis of HFpEF underlines the quasi-normal systolic function (EF > 50%) and allows the discrimination from HF patients with reduced EF (HFrEF) [2,3]. Patients with HFpEF are commonly older than HFrEF patients and often present co-morbidities such as hypertension, obesity, diabetes mellitus, anemia, and atrial fibrillation.

---

[*] Corresponding author at: Inserm 1046 - UMR CNRS 9214 – Université de Montpellier, Physiologie et Médecine Expérimentale du Cœur et des Muscles, CHU Arnaud de Villeneuve, Bâtiment Crastes de Paulet, 371 avenue du doyen Gaston Giraud, 34295 Montpellier Cedex 5, France.

E-mail addresses: charlotte.farah@uclouvain.be (C. Farah), amanda.finan-marchi@inserm.fr (A. Finan), patrice.bideaux@inserm.fr (P. Bideaux), valerie.scheuermann@inserm.fr (V. Scheuermann), youakim.saliba@usj.edu.lb (Y. Saliba), cyril.reboul@univ-avignon.fr (C. Reboul), olivier.cazorla@inserm.fr (O. Cazorla), franck.aimond@inserm.fr (F. Aimond), sylvain.richard@inserm.fr (S. Richard), jerome.thireau@inserm.fr (J. Thireau), nassim.fares@usj.edu.lb (N. Fares).

[1] These authors contributed equally to this work.

Diastolic dysfunction in HFpEF has been frequently associated with LV hypertrophy in response to systemic hypertension [5,6]. A specific, effective therapy has not yet been identified to treat HFpEF [7–9]. Management to delay disease progression is limited to diuretics, treatment of hypertension, and care of lung function abnormalities and other comorbidities [7,10–12]. Identification of targetable mechanisms involved in the pathogenesis and progression of HFpEF is still a major challenge [13].

The heart of HFpEF patients exhibits structural alterations including cardiac hypertrophy, interstitial fibrosis, and coronary capillary rarefaction [14]. These alterations may contribute to increased LV passive stiffness, impaired relaxation, elevated LV end-diastolic pressure, and enlarged left atrium (LA) due to increased filling pressures [3,4,15]. The underlying mechanisms are diverse and complex, involving systemic inflammation, oxidative stress, coronary microvascular endothelial dysfunction, infiltration by activated macrophages, reactive interstitial fibrosis, changes in the extracellular matrix, and modifications in the phenotype of cardiomyocytes resulting from the myocardial remodeling [9]. Changes in both collagen and titin organization/structure/isoform contribute to the development of passive stiffness [16]. Hypophosphorylation of myofilament proteins and increased Ca^{2+} sensitivity have also been reported, suggesting that functional impairment at the cardiomyocyte level is an early event [17]. Abnormal intracellular Ca^{2+} cycling, in relation with impaired intracellular Ca^{2+} decline following systole and diastolic Ca^{2+} overload, respectively, may also compromise relaxation and myocyte stiffness [18,19]. The purpose of this study was to investigate the cellular phenotype and Ca^{2+} handling mechanisms in an experimental model presenting common characteristics of HFpEF and relevant to systemic hypertension. This approach provided a unique access to cellular and molecular functions not accessible in human. Four weeks after surgery, a portion of rats submitted to chronic pressure overload induced by abdominal aortic banding (AAB), recapitulated criteria of preclinical models of HFpEF [20] including lung congestion, concentric hypertrophy, increased LV mass, impaired active relaxation, impaired passive filling, enlarged LA, and cardiomyocytes hypertrophy. The results show stronger contraction of LV myocytes associated with critical alterations in Ca^{2+} cycling and opposing effects on various Ca^{2+} handling proteins possibly to maintain normal contraction.

2. Materials and methods

2.1. Experimental model of chronic pressure-overload

Male *Wistar* rats (weight, 150–200 g; 6 weeks) were purchased from Janvier Laboratories (Le Genest-Saint-Isle, France). All protocols complied with Directive 2010/63/EU of the European Parliament and the Council of 22 September 2010 for the protection of animals used for scientific purposes (agreement: A34-172-38; project APAFIS #3428). Animals were housed in a temperature-regulated room (12 h day/12 h night cycle) with *ad libitum* access to food and water. Surgery was performed according to standard procedures. Rats were anesthetized with intraperitoneal ketamine (120 mg/kg) and xylazine (8 mg/kg). The abdominal aorta adjacent to renal arteries was constricted at the suprarenal level by a silk suture ligature to tie off the vessel against a 21-gauge needle that was subsequently removed (AAB group). Sham-operated rats underwent an identical procedure, but without abdominal aorta ligation.

2.2. Echocardiography

Transthoracic echocardiography was performed 4 weeks after surgery using a Vevo 2100 high resolution ultrasound system (Fujifilm Visualsonics), equipped with a 21 MHz transducer. Rats were anesthetized with 2.5% isoflurane in 100% oxygen (heart rate: 353 ± 23 bpm). Left ventricular (LV) parasternal long axis 2D view in M-mode was performed at the level of papillary muscle to assess LV wall thicknesses and internal diameters, allowing the calculation of the fractional shortening (FS) and ejection fraction (EF) by the Teicholz method. The relative wall thickness index (RWT) was calculated as $RWT = (IVSd + PWTd) / LVIDd$ (with IVS: inter-ventricular septum; PWT: posterior wall thickness; LVID: LV internal diameter; d, in diastole). EF was also calculated (%) from a B-mode parasternal long axis view by tracing endocardial end-diastolic and end-systolic borders to estimate LV volumes. To assess LV diastolic function, mitral inflow was recorded by a pulsed-wave Doppler in the apical four-chamber view by placing the sample at the tip of the mitral valves. Peak early (E) and late atrial contraction (A) mitral inflow waves were measured and the E/A ratio was calculated. Mitral valve deceleration time (MV decel), isovolumic relaxation, and contraction times (IVRT and IVCT respectively) as well as the mitral valve ejection time (MV ET) were measured to calculate the myocardial performance index (MPI) as $MPI = (IVRT + IVCT) / MV\ ET$. Tissue Doppler imaging of the mitral annulus was performed to assess the early diastolic myocardial relaxation velocity waves (e'). The E/e' ratio was calculated as an index of the LV filling pressure. The left atrium (LA) diameter was measured in a right parasternal long axis view. Pulsed-wave Doppler of the ascending aortic blood flow was recorded permitting measurement of the velocity time integral (AoVTI). All measurements were quantified and averaged for three cardiac cycles.

2.3. In vivo hemodynamic investigations

Experiments were performed in intact closed-chest rats as described [21,22]. Rats were anesthetized (Isoflurane 1.5–2.5%) and placed in a supine position on an automatic heating pad. Body temperature, measured *via* a rectal probe, was maintained at 37 °C throughout the procedure. Invasive measurements of both arterial and left intraventricular pressure were performed using a 2F microtip pressure catheter (SPR407, Millar Instruments, Houston, Tx) introduced in the right carotid artery. The catheter was subsequently advanced into the LV to measure systolic and end-diastolic pressures. The analog outputs of the arterial pressure and heart rate were collected with an MP35 module (Biopac System, Gotela, Santa-Barbara, CA). Data were processed using BIOPAC Lab Pro 3.7 software.

2.4. Interstitial fibrosis

Quantification of interstitial fibrosis was performed using Masson's trichrome staining of the left ventricle from sham and AAB rats. Cryosections were fixed with 4% PFA (paraformaldehyde) for 1 h at room temperature, followed by incubation in Bouin's solution overnight. The following day, the tissue samples were washed under running tap water for 2 min and rinsed with distilled water. Sections were stained in Harris Hematoxylin solution for 3 min, rinsed under running tap water for 10 min, and then rinsed with distilled water for 1 min. The Biebrich Scarlet-Acid Fuscsin solution was added for 5 min followed by a rinse with distilled water. The stain was differentiated in phosphotungstic/phosphomolybdic acid solution for 10 min; transferred directly into aniline blue solution for 5 min; rinsed with distilled water; differentiated in 1% acetic acid for 1 min, rinsed with distilled water and dehydrated, cleared and mounted on a coverslip.

2.5. Single myocytes isolation

LV cardiomyocytes were isolated by enzymatic digestion as described [23,24]. Briefly, hearts were quickly removed and cannulated through the aorta to a retrograde perfusion Langendorff system. Hearts were perfused with a free Ca^{2+} physiological Tyrode solution (in mM: NaCl, 116; KCl, 6; $NaHCO_3$, 4; KH_2PO_4, 1.5; $MgCl_2$, 1.7; HEPES, 21; taurine 20, and, glucose 12; pH, 7.15) containing a protease inhibitor (E-64d, 10 μM, Sigma-Aldrich, St-Quentin-Fallavier, France) at a constant flow perfusion rate. Hearts were then perfused with type IV collagenase (Worthington, France) solution and LV myocytes collected in a Ca^{2+} free solution, dissected, and mechanically dispersed. The Ca^{2+} concentration was increased gradually to 1 mM and cells maintained in a physiological solution at 37 °C for 30 min before further processing. Only quiescent cells were used for experiments.

2.6. Force measurements in permeabilized cardiomyocytes

Active and passive forces were measured in single permeabilized cardiomyocytes. The procedures have been described [25]. Myocytes were attached to a piezoresistive strain gauge (AE801 sensor, Memscap, Crolle, France) and to a stepper motor driven micromanipulator (MP-285, Sutter Instrument Company, Novato CA, USA) with thin needles and optical glue (NOA 63, Norland products Inc., North Brunswick, NJ) that polymerized with 2 min UV illumination. Sarcomere Length (SL) was determined online throughout the experiment at 50 Hz by using a Fast Fourier Transform algorithm on the video images of the cell. Force was normalized to the cross-sectional area measured by imaging with an IonOptix® system (Milton, MA, USA) connected to an inverted fluorescence microscope. Active and passive forces were measured either by perfusing the cells with different Ca^{2+} containing solutions at a given length (1.9 and 2.3 µm SL) or by stretching the cells from 1.9 to 2.3 µm SL in relaxing solution, respectively [25]. For each cell, the relationship ascribed by sigmoid curves between force and pCa was fitted to the relative force-pCa relationships by non-linear squares analysis. The curves were of a modified form of the Hill equation: relative force = $[Ca^{2+}]^{n}_{H} / (K^{+}[Ca^{2+}]\,{}^{n}_{H})$ where *n*H is the Hill coefficient and K a compound association constant. The pCa_{50}, pCa for half maximal activation, equals $–(\log_{10} K) / {}^{n}_{H}$ [25].

2.7. Cell shortening and calcium transients

Single cell contractility and intracellular Ca^{2+} were measured using the IonOptix® system (Milton, MA, USA) on freshly isolated LV myocytes incubated in a physiological tyrode solution (in mM: NaCl, 140; KCl, 4; $MgCl_2$, 1; HEPES, 5; $CaCl_2$, 1.8; glucose, 11; pH, 7.4). Myocytes were loaded with the ratiometric Ca^{2+} dye indo-1 AM at room temperature for 10 min (2 µM, Life technologies, St-Aubin, France). Cell shortening and Ca^{2+} transients were evoked by means of electrical-field stimulation with 1-ms current pulses delivered *via* two platinum electrodes. Cells were paced at 0.5 Hz during periods of 20 s, followed by 10 s resting periods. This experimental challenge also allowed the assessment of spontaneous Ca^{2+} events, either during pacing or resting periods. We used caffeine (10 mM) to deplete SR Ca^{2+} stores and evaluate SR Ca^{2+} content [26–28]. NCX activity was assessed based on kinetics analysis of the decay of the Ca^{2+} transient evoked by caffeine [26,29]. Cells were stimulated until steady-state twitches and Ca^{2+} transients were achieved. Pacing was discontinued before sustained application of caffeine. The cytosolic Ca^{2+} concentration was obtained by measuring the fluorescence ratio F405/F480. Data were analyzed using IonWizard 6.4 software.

2.8. Ca^{2+} sparks

To observe the activity of RyR2, Ca^{2+} sparks were recorded in quiescent LV myocytes by means of confocal imaging (Zeiss LSM510 Carl Zeiss Inc., Oberkochen, Germany) with a 63× water-immersion objective (NA: 1.2) and use of Ca^{2+} indicator Fluo-4-AM (4 µM) (Molecular Probes, USA). The dye was excited at 488 nm and the fluorescence emission was collected through a 505-nm long-pass filter. LV myocytes were field-stimulated at 1 Hz with 1-ms current pulses delivered *via* two platinum electrodes, one on each side of the perfusion chamber. During the rest period that followed stimulation, myocytes were repetitively scanned along the entire length of the cell at 1.5 ms intervals, for a maximum of 6 s. The laser intensity was reduced to 5% maximum to decrease cell damage and dye bleaching. Line scan diagrams were constructed by stacking emission lines, corresponding to excitation scans, in temporal order. An average of the Ca^{2+} sparks was determined by the intensity of each sequential scan line and plotting the mean intensity as a function of time. The SparkMaster plug-in for ImageJ software was used to detect and analyze Ca^{2+} sparks.

2.9. Protein analysis

Proteins were extracted from the LV of Sham and AAB rats. Tissues were lysed in lysis buffer containing Tris maleate 10 mM (pH 6,8), NaF 35 mM, triton 1%, Na_3VO_4 1 mM and protease inhibitors (complete Protease Cocktail inhibitor, ROCHE) and homogenized with a manual polytron® instrument. Then the tissues underwent a rotated agitation for 45 min and the protein concentration was determined with the DC Protein Assay (Biorad, USA). Proteins were separated by 4%–20% gradient sodium dodecyl sulfate– polyacrylamide gel electrophoresis and transferred onto nitrocellulose membranes (GE Healthcare, USA) for 1 h at 100 V. The membranes were blocked and then incubated overnight with primary antibodies NCX (1:1000, SWANT), SERCA2A (1:1000, BADRILLA), PLN (1:1000, ABCAM), anti-PLN phospho-Thr17 (1:1000, BADRILLA), RyR (1:500, ABCAM), SNO RyR (1:1000, ABCAM), anti-RyR2 phospho-Ser2814, 1:500 (produced against RyR2 phospho-Ser2814 in rabbit), and FKBP12.6 (1:500, ReD SYSTEM) at 4 °C. An anti-RyR antibody (ABCAM) was used to immunoprecipitate RyR2 to analyze RyR2 S-nitrosylation and FKBP12.6. The samples were incubated with the antibody and RIPA buffer (10 mMTris-HCl (pH 7.4), 150 mM NaCl, 1% Triton- ×100 5 mM NaF, 1 mM Na3VO4, and protease inhibitors) for 1 h at 4 °C. The immune complexes were incubated with protein G Sepharose beads (Sigma-Aldrich) at 4 °C for 1 h. Proteins were separated on SDS/PAGE. The protein levels were expressed relative to Tubulin content using anti-Tubulin (1:1000, Santa Cruz Biotechnology). Immunodetection was carried out using specific fluorescent (infrared-labeled) secondary antibodies and the immunoblots developed were quantified with the Odyssey infrared imaging system (LI-COR Biosystems, USA).

2.10. Cellular electrophysiological recordings

Whole-cell patch clamp recordings were performed on single LV myocytes using an Axopatch 200B amplifier (Axon Instruments), interfaced to a Dell microcomputer with a Digidata 1440A Series analog/digital interface (Axon), and pClamp 10 (Axon) software. Recording pipettes ($\approx 2\,M\Omega$) were filled with a Ca^{2+} rich (100 nM free Ca^{2+}) intracellular solution containing (in mmol/L): KCl 120; EGTA 8; HEPES 10; $MgCl_2$ 6.8; $CaCl_2$ 3; $ATPNa_2$ 4 and $GTPNa_2$ 0.4 (pH 7.2). The bath solution contained (in mmol/L): NaCl 130; KCl 4; MgCl2 1.8; CaCl2 1.8; HEPES 10; glucose 11 (pH 7.4). In the current-clamp mode, action potentials (AP) were evoked by brief (1–2 ms) depolarizing current injections delivered at 1 Hz. Resting membrane potential, AP amplitude and AP durations at 20% (APD20), 50% (APD50) and 90% (APD90) repolarization were measured. In the voltage-clamp mode, outward voltage-gated outward K^+ currents were evoked during 4.5 s voltage steps to potentials between -40 and $+50$ mV (10 mV increment) from a holding potential (HP) of -80 mV. The inward rectifying K^+ current, I_{K1}, was recorded by 450 ms depolarizations between -120 and -40 mV (10 mV increment) from a HP of -80 mV. Leak currents (< 10 pA) were not corrected. Current amplitudes were normalized to whole-cell membrane capacitance, and current densities (pA/pF) are reported. Data were compiled and analyzed using Clampfit 10.2 (Axon Instruments).

2.11. Statistical analysis

All numerical data are given as mean ± SEM. Statistical analyses were performed using GraphPad Prism (GraphPad Prism 5.01 for windows). Student *t*-test was used for the comparison of two groups. The number of arrhythmic cells data was analyzed by Fisher's exact test. A p value ≤ 0.05 was determined as statistically significant.

3. Results

3.1. Heart function and morphology

Six week-old male *Wistar* rats were submitted to AAB-induced pressure overload and compared to age-matched Sham animals following the protocol shown in supplementary Fig. S1. Invasive hemodynamic measurements 4 weeks after surgery confirmed that AAB resulted in increased systolic, diastolic and mean arterial blood pressures in intact closed-chest anesthetized rats (supplementary Fig. S2). These increases were associated with a marked increase in LV end-diastolic pressure and LV end-systolic pressure. Both the heart weight-to-body weight (HW/BW) and the heart weight-to-tibia length ratios (HW/TL) were also increased in AAB rats (Table 1). Signs of cardiac interstitial fibrosis were observed in some, but not all, hearts from AAB rats, suggesting that the fibrotic process was not yet fully established (supplementary Fig. S3).

Follow-up of heart morphology and functional evaluation by Doppler echocardiography and Tissue Doppler Imaging (TDI) revealed that four weeks after surgery was the minimal time required for the animals to develop features of HFpEF after AAB. This time point was thus chosen for experimental investigations. We excluded AAB animals (15/44) with an EF < 55% to ensure a margin threshold for further investigation [20]. The remaining AAB animals (29/44) still exhibited a concentric hypertrophy characterized by increases in LV posterior wall thickness (Table 2) and relative wall thickness (RWT) index (Fig. 1A). Noteworthy, AAB animals presented a nearly normal EF (Sham: 71 ± 2%, n = 16; AAB: 62 ± 2%, n = 29; see Table 1) and velocity time integral of the ascending aortic blood flow (AoVTI) reflecting cardiac output (Fig. 1B,C).

To evaluate diastolic function, we investigated sensitive characteristics of the transmitral inflow pattern. The E/A ratio, reflecting the early passive (E-wave) and late atrial contraction (A-wave) components of the LV filling, was unchanged in AAB *vs*. Sham (Fig. 1D), possibly reflecting an intermediate stage with both impaired LV relaxation and reduced filling in diastole (trend to decrease) and opposing increase in left atrial (LA) pressure (pseudo-normalization). The LV filling inflow waves profile was clearly modified, with an increase of the velocity of both the E and A waves (Fig. 1E–F) and a decrease of the mitral valve deceleration time (Fig. 1G). In some AAB animals, a total fusion of the E wave with the A wave was observed (Fig. 1H, bottom panel), indicating LV filling deterioration. The isovolumic relaxation time (IVRT) was prolonged indicating impaired LV relaxation (Fig. 1I). The isovolumic contraction time (IVCT; Table 1) was increased, likely resulting from aortic constriction-induced increase of the post-charge. Consequently, the myocardial performance index (MPI or Tei Index = (IVRT + IVCT) / mitral valve ejection time), notably used to assess global heart dysfunction and for prognostic information in patients with HFpEF [30,31], was increased (Fig. 1J). The LA pressure was also higher in AAB hearts, as indicated by the increase in the E/e' ratio (peak mitral inflow velocity/tissue Doppler peak diastolic mitral annulus velocity) (Fig. 1K). Due to chronic pressure, the LA was dramatically enlarged in AAB hearts (Fig. 1L), as expected for compensation of LV relaxation impairment and increased LV filling pressure. The lung weight-to-body weight ratio (LW/BW), a sensitive marker for pulmonary edema, was also increased (Table 1) despite preserved fractional shortening, consistent with a HFpEF status [32]. Therefore, 4 weeks post-surgery, our AAB model presented signatures in line with HFpEF abnormalities of active relaxation and passive ventricular filling and pseudo-normal systolic function. Thus, we ensured that all of the AAB animals investigated further at the cellular level had echocardiographic signatures of HFpEF to enhance robustness of the model.

Table 1
Cardiac hypertrophy and lung congestion 4 weeks after AAB.

	Sham (N = 16)	AAB (N = 29)
HW/BW (g/kg)	0.04 ± 0.01	0.06 ± 0.02[***]
HW/TL (g/cm)	0.45 ± 0.01	0.65 ± 0.02[***]
LW/BW (mg/g)	3.0 ± 0.1	3.5 ± 0.05[*]

HW: heart weight; BW: body weight; LW: lung weight; TL: tibia length. Results are expressed as mean ± SEM. Student *t*-test was used to compare groups. AAB *vs*. Sham.

[*] $p < 0.05$.

[***] $p < 0.001$.

Table 2
Evaluation of heart morphology and function by transthoracic echocardiography 4 weeks after AAB.

	Sham (N = 16)	AAB (N = 29)
LV morphology and Systolic function		
HR (bpm)	362 ± 4	348 ± 5[*]
IVSs (mm)	2.8 ± 0.09	3.2 ± 0.06[***]
LVIDd (mm)	8.0 ± 0.13	8.4 ± 0.14[*]
LVIDs (mm)	4.6 ± 0.13	5.5 ± 0.15[***]
PWTd (mm)	1.8 ± 0.05	2.3 ± 0.07[***]
PWTs (mm)	2.9 ± 0.06	3.3 ± 0.09[***]
EF (%)	71 ± 1	62 ± 2[***]
FS (%)	42 ± 1	35 ± 1[***]
EF (%) B-mode	74 ± 1	65 ± 2[***]
RWT	0.44 ± 0.01	0.52 ± 0.01[***]
Ao VTI (mm)	83 ± 2	77 ± 2[*]
Diastolic function		
E wave (mm/s)	987 ± 32	1163 ± 37[**]
A wave (mm/s)	712 ± 33	925 ± 88[***]
E/A	1.4 ± 0.1	1.3 ± 0.1
MV Decel (ms)	33 ± 1	28 ± 1[*]
IVCT (ms)	16 ± 1	23 ± 2[**]
IVRT (ms)	16 ± 1	22 ± 1[***]
MV ET (ms)	58 ± 2	63 ± 1[*]
MPI	0.56 ± 0.03	0.73 ± 0.05[*]
e' wave (mm/s)	64 ± 5	64 ± 5
E/e'	16.3 ± 1.2	21.2 ± 1.8[*]
LA (mm)	4.8 ± 0.1	6.1 ± 0.2[***]

HR: heart rate; IVSd: Inter-ventricular septum thickness in diastole; IVSs: Inter-ventricular septum thickness in systole; LVIDd: left ventricular internal diameter in diastole; LVIDs: left ventricular internal diameter in systole; PWTd: posterior wall thickness in diastole; PWTs: posterior wall thickness in systole; EF: ejection fraction measured by Teicholz method; FS: fractional shortening measured by Teicholz method; EF B-mode: ejection fraction measured by Simpson method in B-mode; RWT: relative wall thickness, calculated as RWT = (IVSd + IVSs) / LVIDd; Ao VTI: aortic flow velocity time integral; E wave: peak velocity of early left ventricular filling wave; A wave: peak velocity of late atrial contraction left ventricular filling wave; E/A: ratio of E wave on A wave; MV Decel: mitral valve deceleration time; IVCT: isovolumic contraction time; IVRT: isovolumic relaxation time; MV ET: mitral valve ejection time; MPI: myocardial performance index, calculated as MPI = (IVRT + IVCT) / MV ET; e' wave: early diastolic mitral annulus tissue velocity peak; E/e': ratio of E wave on e' wave; LA: left atrium diameter. Results are expressed as mean ± SEM. Student *t*-test was used to compare groups. AAB *vs*. Sham.

[*] $p < 0.05$.

[**] $p < 0.01$.

[***] $p < 0.001$.

3.2. Force generation in single cardiomyocytes

We investigated both the Ca^{2+}-activated force and the passive force of single, permeabilized LV myocytes as described [23,33]. The relationship established between the Ca^{2+} concentration and the Ca^{2+}-activated force showed no difference in the maximal isometric tension normalized to the cross-sectional area in AAB animals compared to

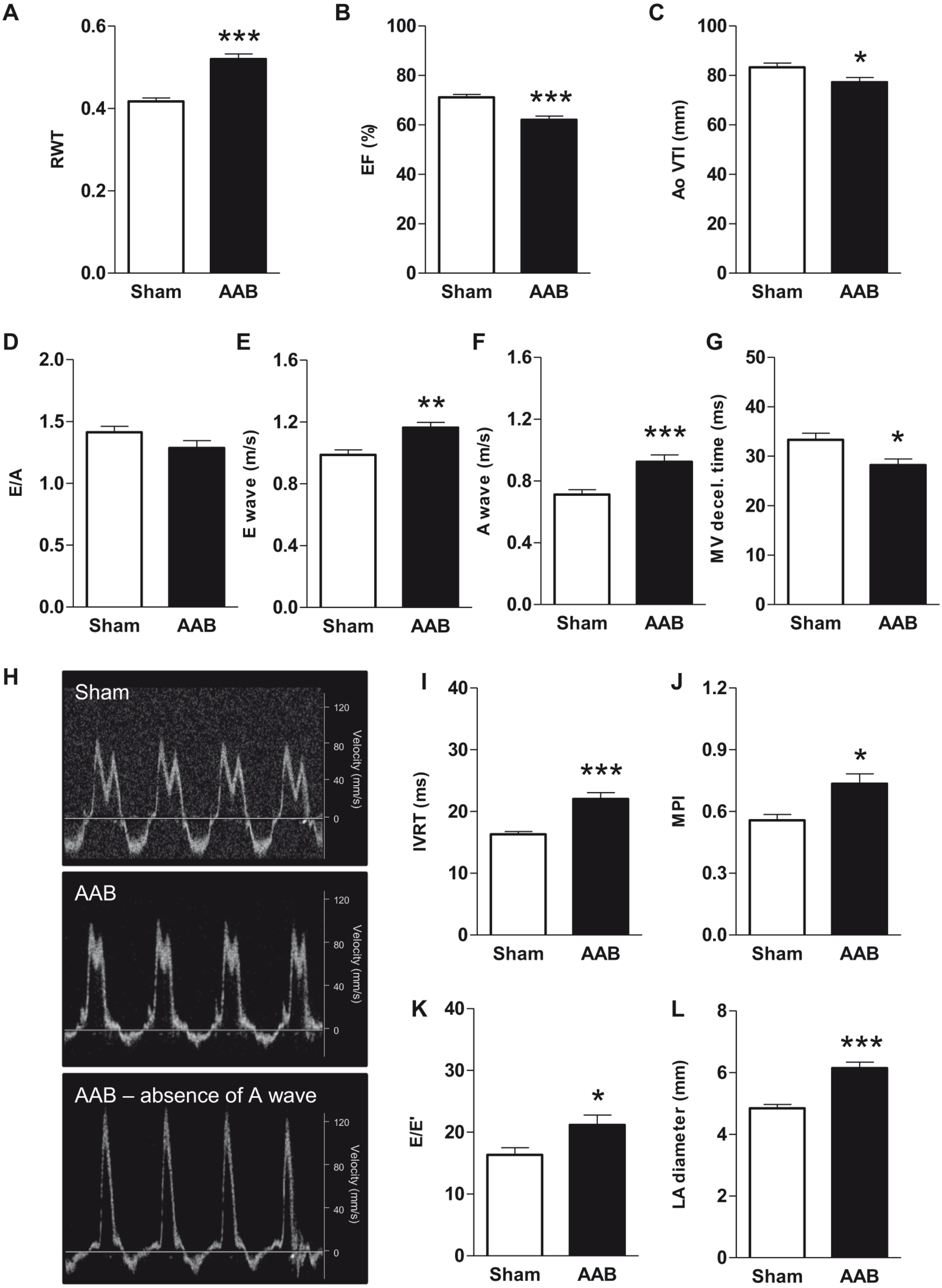

Fig. 1. Left ventricle morphology and function determined by transthoracic echocardiography in AAB rats 4 weeks post-surgery. (A) Relative wall thickness (RWT = anterior wall thickness in diastole (AWTd) + posterior wall thickness in diastole (PWTd)/Left ventricular internal diameter in diastole (LVIDd)). (B) Ejection fraction (EF); (C): Aortic velocity time integral (Ao VTI). (D) Ratio of early mitral inflow wave velocity peak (E) on atrial contraction inflow wave velocity peak (A). (E) Early mitral inflow wave velocity peak (E); (F) Atrial contraction inflow wave velocity peak (A). (G) Mitral valve deceleration time (MV decel.). (H) Illustrations of mitral blood inflow waves in M-mode view. (I) Isovolumic relaxation time (IVRT). (J) Myocardial performance index (MPI = (IVRT + IVCT) / mitral valve ejection time (MV ET)). (K) Ratio of E wave on early diastolic mitral annulus tissue velocity peak E' (E/e'). (L) Left atrium (LA) diameter. Results are expressed as mean ± SEM for Sham rats (N = 16), and AAB rats (N = 29). Student *t*-test was used to compare the two groups. $^{*}p < 0.05$, $^{**}p < 0.01$, $^{***}p < 0.001$, AAB *vs.* Sham.

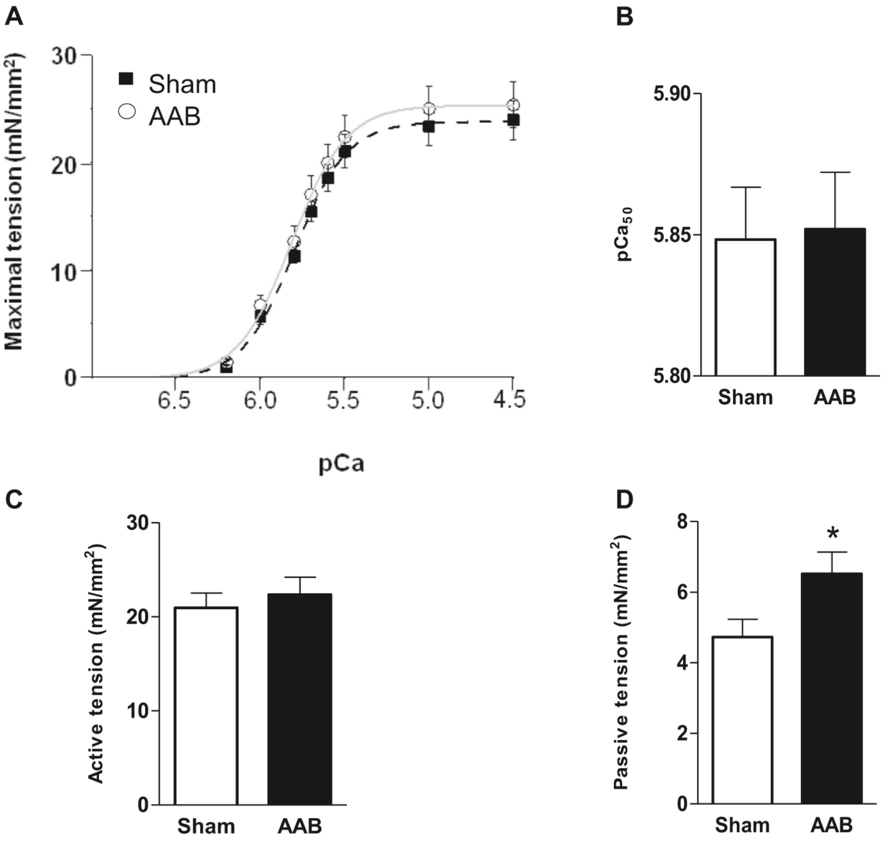

Fig. 2. Maximal active and passive tensions of permeabilized LV myocytes from AAB rats. (A) Relationship between maximal Ca^{2+}-activated tension (mN/mm^2) and intracellular Ca^{2+} measured at 2.3 µm sarcomere length. (B) The pCa at which half the maximal tension developed (pCa_{50}, where $pCa = -\log_{10}[Ca^{2+}]$) determines an index of myofilament Ca^{2+} sensitivity. (C) Active tension. (D) Passive tension. Results are expressed as mean ± SEM for Sham n = 21 cells and AAB n = 20 cells from 4 hearts each. Student *t*-test was used to compare the two groups. $^*p < 0.05$, AAB *vs*. Sham.

Sham. The steepness of tension-pCa curves (modified nHill coefficient), the pCa_{50} and the maximal Ca^{2+}-activated tension were similar in AAB and Sham animals, (Fig. 2A–C) indicating that, for a given amount of Ca^{2+}, the force generated by the myofilaments was unchanged. By contrast, the passive tension developed by myocytes after a stretch at the same sarcomere length (SL) was higher in the AAB group than in the Sham group (Fig. 2D), highlighting stiffer cardiomyocytes in AAB animals.

3.3. Cell contraction and Ca^{2+} handling in single cardiomyocytes

We evaluated excitation-contraction coupling (ECC) by assessing the relationship between SL variations and intracellular Ca^{2+} transients in paced single intact LV myocytes. In the AAB group (*vs*. Sham), the resting SL was unchanged (Fig. 3A, B) whereas SL shortening, an index of contraction, was increased (Fig. 3C). In line with this higher contractile performance, the velocity of cell contraction, calculated by the first derivative of cell shortening (delta SL/delta time), was increased (Fig. 3D) while the velocity of relaxation was unchanged (Fig. 3E). This positive inotropy was associated with an increase in the amplitude of the Ca^{2+} transient (Fig. 3F, G), a delay in the Ca^{2+} transient decay (Fig. 3H) and a moderate elevation of diastolic Ca^{2+} (Fig. 3I). As Ca^{2+} transient amplitude depends on the Ca^{2+} reuptake by the SR, we estimated the SR Ca^{2+} content by triggering maximal Ca^{2+} release instantaneously upon rapid caffeine application (10 mM) (Fig. 3J). Sustained caffeine application evoked Ca^{2+} transients of comparable amplitude in the Sham and AAB groups (Fig. 3K), suggesting similar SR Ca^{2+} content in the two groups. However, the decay was slower in the AAB group (4.82 ± 0.62 s, n = 19) than in the Sham group (2.66 ± 0.18 s, n = 13; p = 0.009; Fig. 3J, L). Taken together, these data underscore significant functional modifications of the ECC and of Ca^{2+} handling in LV cardiomyocytes from AAB animals 4 weeks after surgery.

3.4. Abnormal Ca^{2+} transients and spontaneous Ca^{2+} waves in single cardiomyocytes

We paced indo-loaded LV myocytes with trains of stimulation at 0.5 Hz, interrupted by resting periods to simulate a relaxing state. During pacing, all cells exhibited spatially uniform Ca^{2+} transients in the Sham group whereas AAB cells showed irregular Ca^{2+} transients in 16% of cells (Fig. 4A). During diastolic periods, abnormal events seen as spontaneous Ca^{2+} waves occurred (Fig. 4B). While this type of event was rare in the Sham group (3% of cells), spontaneous Ca^{2+} waves occurred in nearly half of the cells (46%) from the AAB group, underscoring dynamic instabilities in Ca^{2+} cycling (Fig. 4B). Spontaneous Ca^{2+} waves during diastolic periods can result from abnormal openings of the ryanodine receptor 2 (RyR2) generating microscopic Ca^{2+} events referred to as Ca^{2+} sparks [34–37]. We visualized Ca^{2+} sparks by means of confocal microscopy using the fluorescent Ca^{2+} indicator Fluo-4 to evaluate the leakiness of RyR2. AAB cardiomyocytes had an increase of Ca^{2+} spark frequency compared to Sham (Fig. 4C). Irregular Ca^{2+} transients, abnormal Ca^{2+} waves in diastole, and a higher frequency of Ca^{2+} sparks through RyR2 further confirmed alterations of Ca^{2+} handling in AAB cardiomyocytes.

We next explored the expression of proteins potentially implicated in the modifications of Ca^{2+} handling and the promotion of abnormal spontaneous Ca^{2+} events in AAB rats (Fig. 5). The sarcoplasmic/endoplasmic reticulum Ca^{2+} ATPase (SERCA2a), the phospholamban (PLN) and the Sodium/Calcium exchanger (NCX) protein levels were not significantly modified in AAB hearts (Fig. 5A–D). By contrast, the phospholamban (PLN) to SERCA2a ratio was augmented (Fig. 5E), reflecting an inhibitory effect on the SERCA2a activity. However, PLN phosphorylation at the calmodulin-dependent kinase II (CaMKII)-specific site (PLN-Thr17), which promotes SERCA2A activity, was increased as well (Fig. 5F). The RyR2 protein and its post-translational modifications have been largely implicated as one of the molecular mechanism(s) responsible for the higher occurrence of Ca^{2+} sparks. In

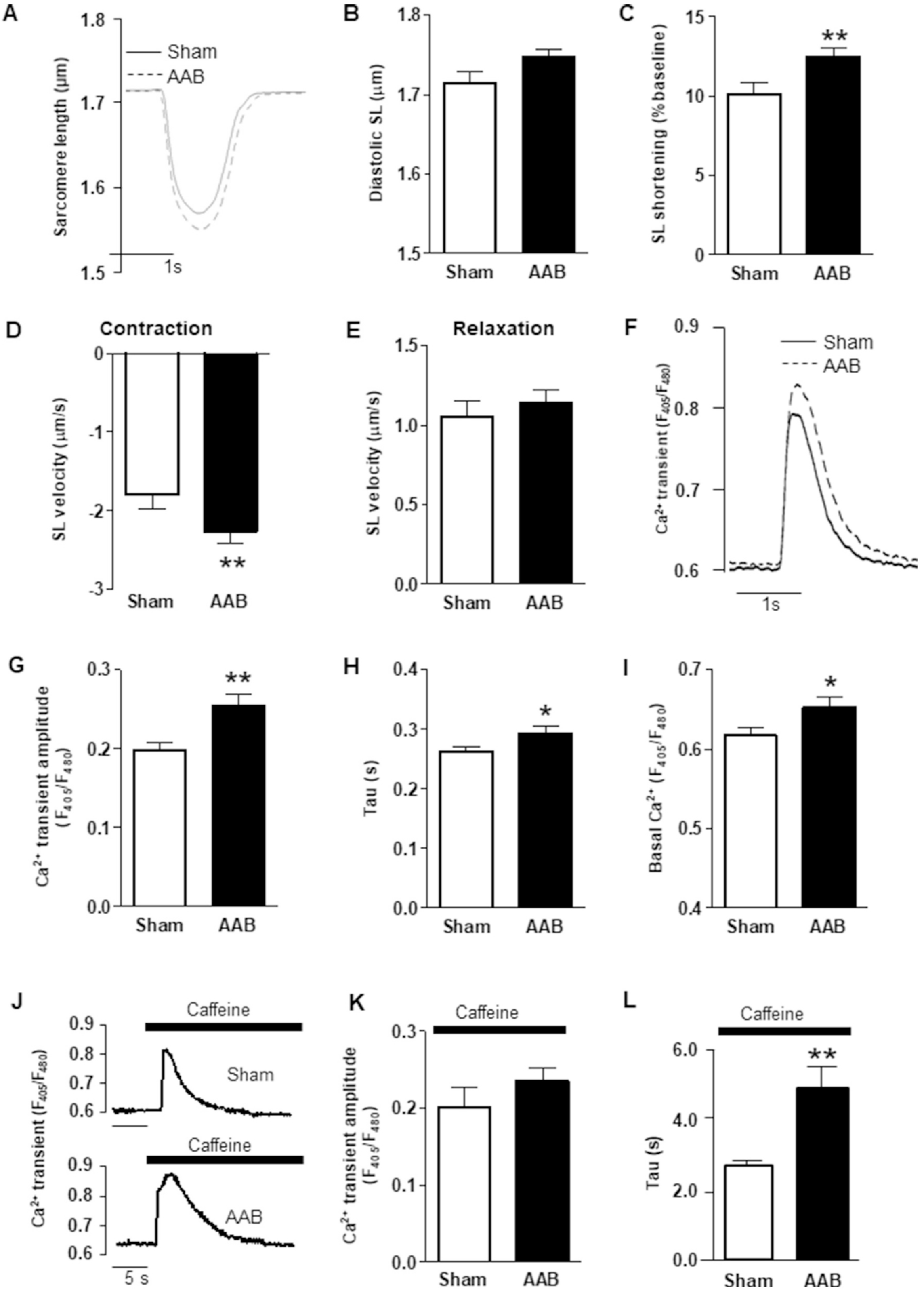

Fig. 3. Enhanced contraction and modified Ca^{2+}handling in intact LV myocytes from AAB rats. (A) Representative contraction evoked by electrical field stimulation as measured from sarcomere length (SL) shortening at 0.5 Hz in intact LV myocytes. (B) Diastolic SL. (C) Shortening during contraction. (D) Contraction velocity. (E) Relaxation velocity; (F) Representative Ca^{2+} transients evoked by electrical field stimulation in intact LV myocytes loaded with indo-1 AM. (G) Ca^{2+} transient amplitude. (H) Ca^{2+} transient decay. (I) Diastolic intracellular Ca^{2+}. (J) Transient increases in intracellular Ca^{2+} triggered by caffeine (10 mM) application. (K) Amplitude of the Ca^{2+} rise triggered by caffeine. (L) Decay of the Ca^{2+} transient evoked by caffeine.

In all panels, results are expressed as mean ± SEM. In panels A–I, for Sham, n = 29 cells (6 hearts); for AAB, n = 37 cells (7 hearts). In panel K and L, for Sham, n = 13 cells (5 hearts); for AAB, n = 19 cells (6 hearts). Student *t*-test was used to compare the two groups. $p < 0.05$, $^{**}p < 0.01$, AAB *vs*. Sham.

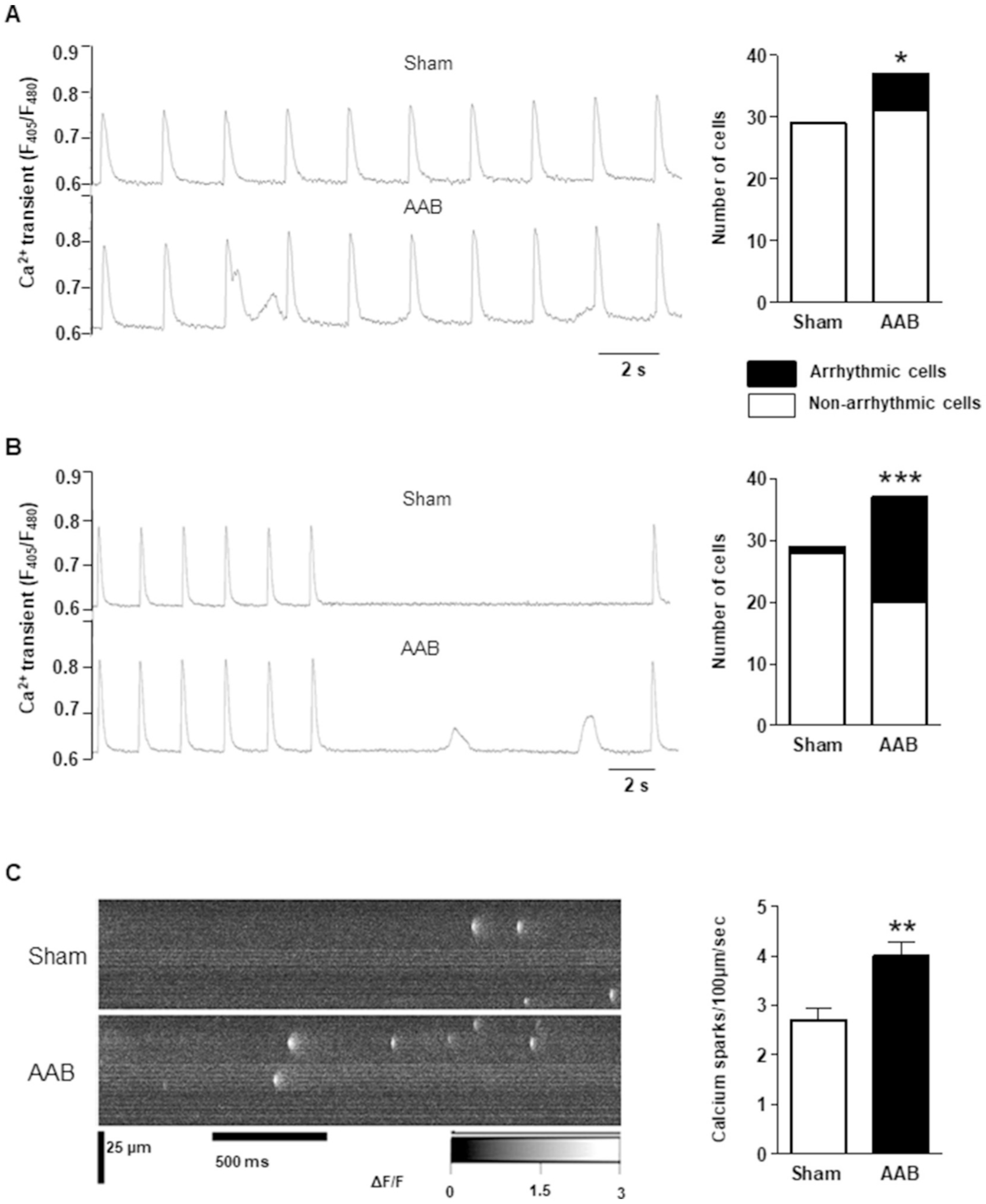

Fig. 4. Irregular Ca^{2+} transients, abnormal Ca^{2+} waves, and a high occurrence of Ca^{2+} sparks in intact LV myocytes from AAB rats. (A) Representative Ca^{2+} transients evoked during pacing in LV cardiomyocytes freshly isolated from Sham and AAB rats; Right panel: total number of cells recorded (white), number of cells with at least one irregular Ca^{2+} transient during the pacing period (black). (B) Spontaneous Ca^{2+} waves during a resting (or quiescent) period in LV cardiomyocytes freshly isolated from Sham and AAB rats; Right panel: total number of cells recorded (white), number of cells with at least one abnormal Ca^{2+} wave (black). In A and B panels, results are expressed as total number of cells for Sham n = 29 cells (6 hearts) AAB n = 37 cells (7 hearts). Fisher's exact test was used to compare the two groups. * $p < 0.05$, *** $p < 0.001$, AAB *vs*. Sham. (C) Left panel: typical line-scan confocal images of spontaneous Ca^{2+} sparks recorded in a line-scan mode in Fluo-4 AM loaded LV cardiomyocytes; right panel: mean frequency of Ca^{2+} sparks measured for Sham n = 22 cells (N = 3 hearts) and AAB n = 27 cells (4 hearts). Student *t*-test was used to compare the two groups. **$p < 0.01$, AAB *vs*. Sham.

AAB hearts, RyR2 protein expression was unchanged and no modifications in the phosphorylation at the CaMKII site (Ser2814), the FKBP12.6/RyR2 ratio, and the S-nitrosylation of RyR2 could be detected (Fig. 5G–J).

3.5. *Action potential and cellular electrical activity*

An essential parameter for the excitation-contraction coupling is cellular electrical activity. We recorded action potentials (AP) and whole-cell ionic currents by means of the patch-clamp technique in single LV myocytes. Cell capacitance, an indicator of cell size, was increased (Fig. 6A) in line with an increase of cell area (supplementary Fig. S4). In AAB LV myocytes, the AP waveform was not substantially modified (Fig. 6B,C) in contrast with the marked prolongation of the repolarizing plateau phase in various models of HF [38–41], yet both a prolongation of the late repolarization (APD90) and a slight depolarization of the resting membrane potential were observed (Fig. 6C). Cardiac AP repolarization is driven by K^+ currents. Fig. 6D shows typical K^+ currents recorded in voltage-clamp conditions in the presence of inward Na^+ and Ca^{2+} current inhibitors [38]. In line with the lack of

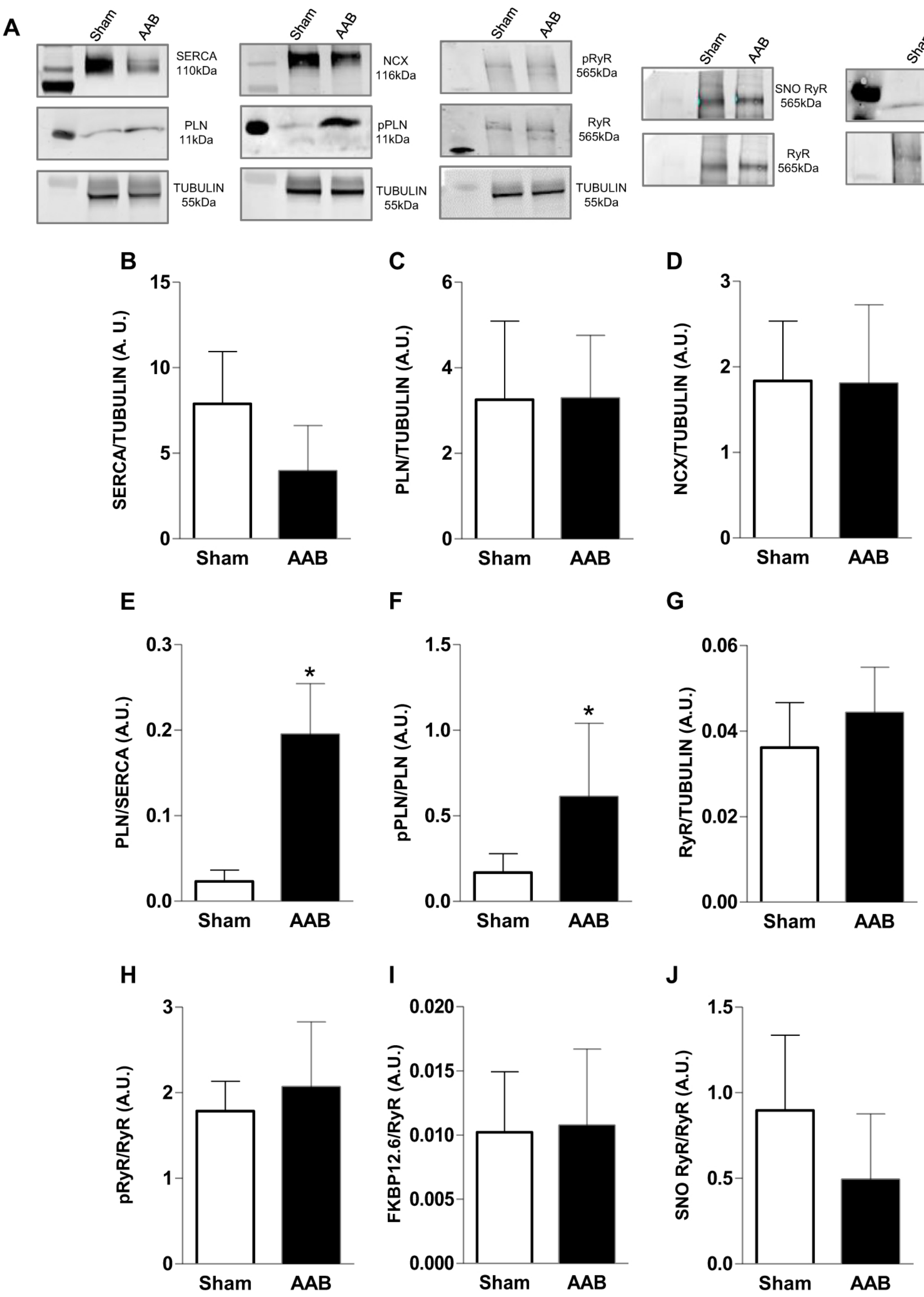

Fig. 5. Expression of Ca^{2+} handling proteins in the LV of AAB rats 4 weeks post-surgery. Western blots and overall results of experiments showing: (A) representative bands for each protein analyzed, (B) the expression of SERCA2a, (C) the expression of PLN, (D) the expression of the Sodium/Calcium exchanger (NCX), (E) the PLN to SERCA2a ratio, (F) the CaMKII-phosphorylated (Thr17)-PLN to PLN ratio, (G) the expression of the Ryanodine Receptor (RyR2), (H) the CaMKII–phosphorylated (Ser2814) RyR2 to RyR2 ratio, (I) the FKBP12.6 to RyR2 ratio, and (J) the S-nitrosylated RyR2 to RyR2 ratio. Protein levels were normalized to Tubulin content. The analyses were performed using Odyssey 3.0 image analysis software (LI-COR Biosciences). The blots are representative of 3 independent experiments (made in triplicate) using 3 hearts for the Sham group and 3 hearts for the AAB group. Student *t*-test was used to compare the two groups. $^{*}p < 0.05$, AAB *vs.* Sham.

effect on the AP plateau, the main I_{to} and I_{sus} K^{+} currents were similar in AAB and Sham. However, I_{K1} contributing to the resting membrane potential and the late repolarization of the AP was reduced at potentials close to the resting membrane in AAB cardiomyocytes (Fig. 6E), which could result from elevated diastolic Ca^{2+}.

4. Discussion

In this study, we show that adaptive modifications of Ca^{2+} cycling through the hypertrophic response to chronic high blood pressure overload play a critical role during early development of heart failure with nearly-normal ejection fraction (HFpEF). Four weeks after AAB, rat hearts were characterized by an increase of LV mass and concentric LV hypertrophy, a preserved systolic function, and other criteria used for preclinical models of HFpEF including elevated blood pressure, lung congestion, impaired active relaxation, impaired passive filling, enlarged left atrium, and cardiomyocyte hypertrophy [20]. We relied on all of these criteria to ensure investigations on a homogenous population of animals. This approach provided unique access to cardiac cellular and molecular functions not accessible in human patients. The AAB animals presented stiffer cardiomyocytes with stronger contraction and increased Ca^{2+} transient. Ca^{2+} cycling was characterized by SR

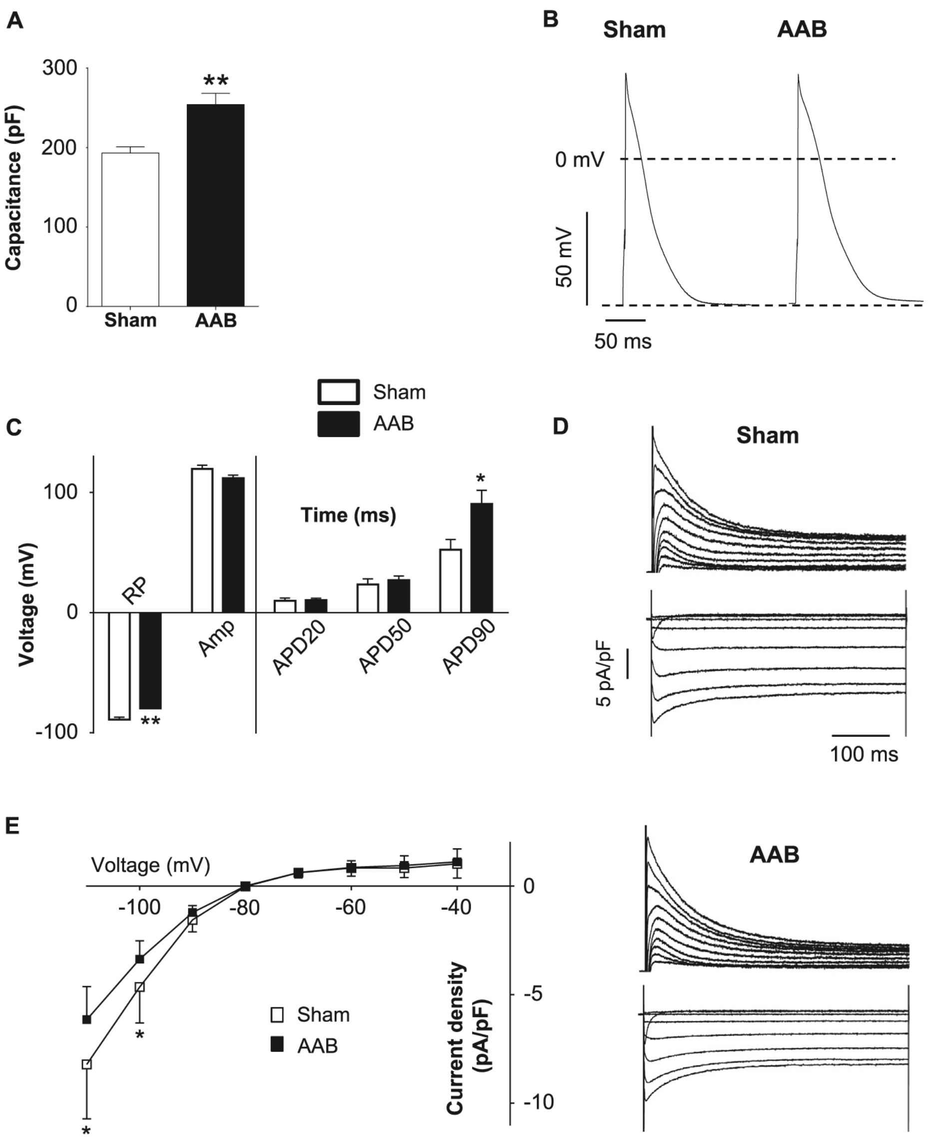

Fig. 6. Electrophysiological properties of LV myocytes from AAB rats. (A) Cell capacitance (in pF) of single myocytes from Sham ($n = 15$) and AAB ($n = 17$). (B) Representative action potential (AP) waveforms recorded in single LV myocytes isolated from Sham (left) and AAB (right) rats. (C) AP properties in Sham ($n = 15$) and AAB ($n = 15$). (D) Representative inward and outward voltage K^+ current recorded from LV myocytes isolated from Sham (top) and AAB (bottom) rats. RP: resting potential (mV); Amp: AP amplitude (mV); APD20, 50, 90: AP durations at 20%, 50% or 90% repolarization (ms). (E) Mean density-to-voltage relationships for I_{K1} recorded in single myocytes from Sham ($n = 14$, white squares) and AAB ($n = 16$, black squares) rats. $^*P < 0.05$; $^{**}P < 0.01$ *vs.* Sham.

Ca^{2+} leak through RyR2, impaired Ca^{2+} extrusion through NCX, and increased PLN/SERCA and pPLN/PLN ratios. The latter protein change may aid in the compensation of the higher PLN/SERCA ratio to rescue SR-Ca^{2+} re-uptake by SERCA2a.

We were able to reproduce clinical facets of HFpEF at a defined time point in the AAB rat model. LV hypertrophy is frequently associated with global diastolic dysfunction and HFpEF in experimental and clinical studies [42]. LV hypertrophy and diastolic dysfunction are common cardiac complications of hypertension, which has stimulated the use of experimental models based on pressure overload [4,5,43–45]. Here, chronic pressure overload promoted early functional and structural cardiac features consistent with HFpEF-like characteristics. Four weeks post-banding, despite only moderate changes in EF, the hearts presented a reduced cardiac performance index (reflected in the increased MPI index) with diastolic dysfunction. The hearts had higher LV filling pressure (estimated by the E/e' ratio), prolonged isovolumic relaxation time (IVRT), and reduced early mitral annulus velocity in line with a rise of LV wall stiffness and impaired active relaxation. These results are consistent with a recent publication on the same model but at a later time point [46]. AAB rats also presented structural, surrogate markers of HFpEF such as concentric LV remodeling and hypertrophy, LA enlargement, and pulmonary edema [20,47–49]. The heterogeneity of interstitial fibrosis among AAB hearts was in line with various degrees of interstitial fibrosis and cardiomyocyte hypertrophy evidenced in HFpEF patients [14,19,50,51]. Fibrosis may develop later, suggesting that early signs of HFpEF both *in vivo* and at the cellular level precede fibrosis. These results, taken together, supported this animal model and our selective approach as a robust method for cellular investigations of HFpEF.

Myocardial remodeling in HFpEF differs from that of HFrEF driven primarily by cardiomyocyte death [52]. Although diastolic dysfunction in HFpEF has multiple origins at non-cardiomyocyte levels [53], cardiac cells are the main effector of the contraction/relaxation cycling involved in proper heart pump function. A major finding in our study was evidence that AAB LV cardiomyocytes had a different functional phenotype than controls and HFrEF, particularly in regards to excitation-contraction coupling. The electrical phenotype of the cardiomyocytes was quasi normal, contrasting with the marked AP plateau prolongation and blunting of repolarizing potassium currents I_K, in particular I_{to}, reported in compensated hypertrophy and/or end-stage failing human, canine and rat hearts [38–41,54,55]. The positive inotropy of the cardiomyocytes also contrasted sharply with the depressed contraction in HFrEF due mainly to reduced Ca^{2+} transient, reflecting lower SR Ca^{2+} content. This is due to depressed SR Ca^{2+} uptake, resulting from blunted SERCA2a activity (reduced SERCA2a protein and dephosphorylated PLN), and SR Ca^{2+} leak through RyR2 channels [56–58].

Despite opposite functional impacts on cell contraction and Ca^{2+} transient, some of the Ca^{2+} cycling defects seen in HF were however identified in our study. They involved delayed Ca^{2+} transient decay, augmented diastolic Ca^{2+}, irregular Ca^{2+} transients during pacing, Ca^{2+} leakage through RyR2 and aberrant spontaneous diastolic Ca^{2+} waves. Although these effects collectively contribute to SR Ca^{2+} depletion and cause defective cardiac excitation-contraction coupling in HFrEF, this was not the case in our model.

The single, hypertrophic, stiffer LV myocytes (Figs. 6A and 2D) unveiled functional modifications including stronger and faster contractions with delayed relaxation (Fig. 3C,D,H). This positive, cellular inotropy was determined primarily by an increase in Ca^{2+} transient amplitude rather than by an amplified Ca^{2+} sensitivity of the contractile proteins. At the cellular level, our findings of stiffer and hypertrophic LV myocytes were consistent with various reports on HFpEF in human and rodents [17,46,50,51,59,60] and explain in part the increased LV wall stiffness and impaired relaxation of the heart. The force developed by the myocytes depends on both the amount of Ca^{2+} released by the SR after excitation and the Ca^{2+} sensitivity of the contractile machinery. Here, single cell contractions were stronger with both a shorter delay for activation and a delayed relaxation, which was consistent with the increased Ca^{2+} transient amplitude and in line with other studies showing enhanced Ca^{2+} mobilization, particularly during early stages of pressure overload-induced hypertrophy [17,61]. Delayed Ca^{2+} extrusion from the cytosol due to impaired NCX activity (Fig. 3J,L) was also a likely contributor. Enhanced Ca^{2+} cycling between the SR and the cytosol was shown to occur even before hypertrophy development, *i.e.* during the very first days following AAB [61]. Here, the positive inotropic-like adaptive effect occurred in absence of marked AP plateau prolongation, as confirmed by a lack of modification in the main repolarizing K^+ currents (except I_{K1}), which was consistent with unchanged L-type Ca^{2+} current. It also did not involve enhanced Ca^{2+} sensitivity of contractile proteins. It remains unclear why the augmented contraction of individual cells did not increase global heart function. Possibilities may include a loss of cardiomyocytes, although this is mainly a HFrEF characteristic, or more likely a variety of non-cardiomyocyte factors as recently reviewed [52].

Four weeks after AAB, Ca^{2+} cycling was characterized by at least four changes occurring in parallel with potentially opposite effects: (i) Ca^{2+} leakage through RyR2 (Fig. 4C); (ii) impaired Ca^{2+} extrusion through NCX (Fig. 3J,L); (iii) increased PLN/SERCA ratio (Fig. 5D), and, (iv) increased pPLN/PLN ratio (Fig. 5E), that may compensate the higher PLN/SERCA ratio to rescue SR Ca^{2+} re-uptake by SERCA2a. Of note, SERCA2a protein abundance was unchanged (Fig. 5A). In normal conditions, Ca^{2+} removal from the cytosol by the SERCA2a pump prevails over NCX activity. As the decline of the Ca^{2+} transient evoked by a caffeine challenge is an index of NCX activity, our results were consistent with an impaired Ca^{2+} extrusion from the cells through the NCX forward mode [62,63]. This was however unrelated to changes in NCX protein expression. Slower decay time of the caffeine-induced Ca^{2+} transient may reflect changes in Na^+ gradient [64] due to elevated intracellular $[Na^+]$ involving possibly factors such as late Na^+ currents, electrogenic Na^+-K^+ ATPase or Na^+ co-transport. Impaired NCX-dependent Ca^{2+} extrusion has been explained by a shift towards an increased reverse mode activity (Ca^{2+} influx), yet this was excluded in a recent study in human hearts of patients with hypertensive heart disease and HFpEF [60,65]. Leaky RyR2 (late Ca^{2+} sparks) [66] associated with both impaired Ca^{2+} extrusion through NCX and increased PLN/SERCA ratio altogether could contribute to the delay in the decay of the Ca^{2+} transient (Fig. 3H) and elevate diastolic Ca^{2+} (Fig. 3I).

PLN has a primary role in the regulation of SERCA2a activity and thereby is a major determinant of cardiac contractility and relaxation. Dephosphorylated PLN inhibits SERCA2a activity whereas PLN phosphorylation at either Ser16 by PKA or Thr17 by CaMKII reverses this inhibition [67]. The PLN/SERCA2a ratio in AAB cardiomyocytes was increased, which is expected to inhibit SERCA2a activity and decrease SR Ca^{2+} reuptake as seen in pathophysiological conditions [68,69]. Remarkably, we detected an increased pPLN/PLN ratio in AAB hearts, *i.e.* PLN was phosphorylated at the CaMKII-specific site (PLN-Thr17). Activation of this CaMKII-specific site (PLN-Thr17) has complex effects. It has been closely associated with an increase in the relaxant effect of a β-adrenergic response [70] but also with reduced β-adrenergic responsiveness in a feline model of chronic pressure overload-induced cardiac hypertrophy [71]. This mechanism may also act as a cardiac beat-by-beat frequency-decoder whereas PKA-mediated phosphorylation (PLN-Ser16) instead responds to exercise, stress or "fight and flight" situations [72]. It may reflect a versatile, adaptive role of PLN and its phosphorylated form to counterbalance impaired NCX activity and RyR2-mediated SR Ca^{2+} leak in an attempt to maintain normal Ca^{2+} cycling in different physiological demands. The exact implications of the increased phosphorylated state of PLN in our model deserve further explorations.

If the cell and the SR are overloaded with Ca^{2+} then abnormal Ca^{2+} transients (Fig. 4A) and spontaneous Ca^{2+} waves (Fig. 4B) are expected to appear [63]. A high occurrence of Ca^{2+} sparks, fueling SR Ca^{2+} leak and cytosolic Ca^{2+} overload, was an unexpected early signature in our model. Late SR Ca^{2+} leak, occurring after an initial slowing of Ca^{2+} transient decay, has been proposed to be a consequence rather than a cause of diastolic dysfunction in a rat model of chronic kidney disease (CKD) with HFpEF [60]. Post-translational modifications of RyR2, such as nitrosylation and CaMKII-dependent phosphorylation, can lead to SR Ca^{2+} leakage [58,73,74] but they were not detected here (Fig. 5). Increased cytosolic Ca^{2+}, in addition to maintained luminal Ca^{2+}, is expected to increase the likelihood of spontaneous release events. Ca^{2+} dependent blockade of the inward rectifier current I_{K1} resulting from the rise in diastolic Ca^{2+} may contribute to the occurrence of the abnormal cellular Ca^{2+} events [24,75,76]. Importantly, the Ca^{2+} leak identified here may not only provide a pro-arrhythmogenic substrate but could also be involved in the progression of HFpEF. Beneficial effects of enhanced SR Ca^{2+} uptake through PLN phosphorylation may be lost when associated with SR Ca^{2+} leak [67]. In addition, Ca^{2+} sensitive signaling factors involved in cardiac hypertrophy are known to respond to sustained changes in diastolic Ca^{2+} concentration [77].

The current study was constrained by a number of limitations. First, the replication of human HFpEF in animal models is difficult. However, there is a need for such investigations with an emerging interest for preclinical models including rodents [20,43,78,79] [80]. A recent review reported a set of clinical criteria helping to define animal models of HFpEF [20], that we applied to this work. Various models of HFpEF exist where both advantages and disadvantages are evident [43]. In particular, the models have different etiologies and temporal progression of the disease. For example, in the comparison of Ca^{2+} handling in different models including human, there are both similarities and disparities underlining complexity and multimodal adaptation to different insults [18,46,60,61,65]. As highlighted by Primessnig and collaborators, "*findings should be interpreted in this context and need to be validated in HFpEF of different aetiology*". A second limitation related to the study is related to neurohormonal activation. This is generally considered a characteristic of systolic HF, but may also be involved in HFpEF [81,82]. There is extensive literature establishing that the renin–angiotensin–aldosterone system (RAAS) plays a role in inducing hypertrophy during pressure overload. Diminished blood pressure distal to the constriction transiently stimulates the secretion of renin to increase blood pressure shortly (3 days) after constriction [83]. Angiotensin receptor inhibition does not reverse the effects of banding, and removal of banding does reduce hypertrophy suggesting that angiotensin does not play a major role in causing pressure overload-induced hypertrophy or in maintaining such hypertrophy [84]. Whether RAAS activation and its extent due to the constriction itself and/or related to the progression of the pathology was involved in our experimental conditions was not investigated in the current study. Third, despite a trend, we found no statistical difference in the amplitude of caffeine-evoked Ca^{2+} transient content between Sham and AAB (Fig. 3K) using caffeine challenge. Indo-1, which we used here, is a high-affinity Ca^{2+} indicator of choice for qualitative comparisons and detection of changes in diastolic Ca^{2+}. However, it may have some limitation for the detection of differences in peak Ca^{2+} between groups in the caffeine experiments. Moderate-affinity dyes, such as the fluo-4 analog fluo-5F, have been preferred by some authors for the detection of variations of cytosolic Ca^{2+} during caffeine challenge [27,29].

In summary, cardiomyocytes, the main effectors of cardiac contraction, play a critical role in a sequence of events induced by chronic cardiac pressure overload triggering concentric hypertrophy, then inducing a heart status recapitulating criteria of HFpEF. We underscored the relationship between early systolic adaptations of Ca^{2+} handling and subsequent maladaptive diastolic changes [42]. We have identified different adaptations of Ca^{2+} handling that may be, presumably, beneficial or detrimental such as impaired NCX activity, Ca^{2+} leak through RyR2 channels dual together with a dual effect on the PLN/pPLN system regulating SERCA2a activity. These effects promote elevated cytosolic Ca^{2+}, which could contribute to impaired relaxation in addition to myocardial stiffness. This may also initiate further deterioration of Ca^{2+} homeostasis in the progression of the disease. This approach here provides an interesting access to identify cellular and molecular dysfunctions not accessible in human with a potential for drug testing. All these aspects warrant further investigation to compare HFpEF of different etiologies [60] and identify the most relevant target proteins.

Transparency document

The Transparency document associated with this article can be found, in online version.

Acknowledgments

We thank the small animal imaging platform of Montpellier (IPAM; http://www.ipam.cnrs.fr) for access to the echocardiography.

Funding sources

This work was supported by the Bilateral Research Collaborative program between France and Lebanon (PHC CEDRE 2015, N° 32955NG to SRo, SRi and NF), the Research Council of Saint Joseph University of Beirut (travel, SRo), the *Fondation de France* (N° 2013-00038586 to SR and JT), and the Bilateral Research Collaborative program CAPES-COFECUB between Brazil and France (n°768/13 to SR; post-doctoral grant to GRdA).

Conflict of interests

None.

References

[1] E. Braunwald, The war against heart failure: the Lancet lecture, Lancet Lond. Engl. 385 (2015) 812–824.

[2] W.J. Paulus, C. Tschöpe, J.E. Sanderson, C. Rusconi, F.A. Flachskampf, F.E. Rademakers, et al., How to diagnose diastolic heart failure: a consensus statement on the diagnosis of heart failure with normal left ventricular ejection fraction by the Heart Failure and Echocardiography Associations of the European Society of Cardiology, Eur. Heart J. 28 (2007) 2539–2550.

[3] P. Ponikowski, A.A. Voors, S.D. Anker, H. Bueno, J.G.F. Cleland, A.J.S. Coats, et al., 2016 ESC Guidelines for the diagnosis and treatment of acute and chronic heart failure: the Task Force for the diagnosis and treatment of acute and chronic heart failure of the European Society of Cardiology (ESC) developed with the special contribution of the Heart Failure Association (HFA) of the ESC, Eur. Heart J. (2016), https://doi.org/10.1093/eurheartj/ehw128.

[4] M.A. Ul Haq, C. Wong, D.L. Hare, Heart failure with preserved ejection fraction: an insight into its prevalence, predictors, and implications of early detection, Rev. Cardiovasc. Med. 16 (2015) 20–27.

[5] F.H. Messerli, S.F. Rimoldi, S. Bangalore, The transition from hypertension to heart failure: contemporary update, JACC Heart Fail. 5 (2017) 543–551.

[6] L.-M. Wu, D.L. An, Q.-Y. Yao, Y.Z. Ou, Q. Lu, M. Jiang, et al., Hypertrophic cardiomyopathy and left ventricular hypertrophy in hypertensive heart disease with mildly reduced or preserved ejection fraction: insight from altered mechanics and native T1 mapping, Clin. Radiol. (2017), https://doi.org/10.1016/j.crad.2017.04.019.

[7] J. Butler, G.C. Fonarow, M.R. Zile, C.S. Lam, L. Roessig, E.B. Schelbert, et al., Developing therapies for heart failure with preserved ejection fraction: current state and future directions, JACC Heart Fail. 2 (2014) 97–112.

[8] J.E. Ho, P. Gona, M.J. Pencina, J.V. Tu, P.C. Austin, R.S. Vasan, et al., Discriminating clinical features of heart failure with preserved vs. reduced ejection fraction in the community, Eur. Heart J. 33 (2012) 1734–1741.

[9] S.J. Shah, D.W. Kitzman, B.A. Borlaug, L. van Heerebeek, M.R. Zile, D.A. Kass, et al., Phenotype-specific treatment of heart failure with preserved ejection fraction: a multiorgan roadmap, Circulation 134 (2016) 73–90.

[10] A.S. Desai, Heart failure with preserved ejection fraction: time for a new approach? J. Am. Coll. Cardiol. 62 (2013) 272–274.

[11] M. Galderisi, Diastolic dysfunction and diastolic heart failure: diagnostic, prognostic and therapeutic aspects, Cardiovasc. Ultrasound 3 (2005) 9.

[12] A.A. Oktay, S.J. Shah, Diagnosis and management of heart failure with preserved ejection fraction: 10 key lessons, Curr. Cardiol. Rev. 11 (2015) 42–52.

[13] S.-H. Wan, M.W. Vogel, H.H. Chen, Preclinical diastolic dysfunction, J. Am. Coll. Cardiol. 63 (2014) 407–416.

[14] S.F. Mohammed, S. Hussain, S.A. Mirzoyev, W.D. Edwards, J.J. Maleszewski, M.M. Redfield, Coronary microvascular rarefaction and myocardial fibrosis in heart failure with preserved ejection fraction, Circulation 131 (2015) 550–559.

[15] L. van Heerebeek, W.J. Paulus, Understanding heart failure with preserved ejection fraction: where are we today? Neth. Hear. J. 24 (2016) 227–236.

[16] M.R. Zile, C.F. Baicu, J.S. Ikonomidis, R.E. Stroud, P.J. Nietert, A.D. Bradshaw, et al., Myocardial stiffness in patients with heart failure and a preserved ejection fraction: contributions of collagen and titin, Circulation 131 (2015) 1247–1259.

[17] N. Hamdani, C. Franssen, A. Lourenço, I. Falcão-Pires, D. Fontoura, S. Leite, et al., Myocardial titin hypophosphorylation importantly contributes to heart failure with preserved ejection fraction in a rat metabolic risk model, Circ. Heart Fail. 6 (2013) 1239–1249.

[18] I. Adeniran, D.H. MacIver, J.C. Hancox, H. Zhang, Abnormal calcium homeostasis in heart failure with preserved ejection fraction is related to both reduced contractile function and incomplete relaxation: an electromechanically detailed biophysical modeling study, Front. Physiol. 6 (2015) 78.

[19] A. Borbély, J. van der Velden, Z. Papp, J.G.F. Bronzwaer, I. Edes, G.J.M. Stienen, et al., Cardiomyocyte stiffness in diastolic heart failure, Circulation 111 (2005) 774–781.

[20] M. Valero-Muñoz, W. Backman, F. Sam, Murine models of heart failure with preserved ejection fraction: a ‘fishing expedition’, JACC Basic Transl. Sci. 2 (2017) 770–789.

[21] D. Vitiello, J. Boissière, G. Doucende, S. Gayrard, A. Polge, P. Faure, et al., β-Adrenergic receptors desensitization is not involved in exercise-induced cardiac fatigue: NADPH oxidase-induced oxidative stress as a new trigger, J. Appl. Physiol. (1985) 111 (2011) 1242–1248.

[22] I. Mercier, M. Pham-Dang, R. Clement, H. Gosselin, F. Colombo, J.-L. Rouleau, et al., Elevated mean arterial pressure in the ovariectomized rat was normalized by ET(A) receptor antagonist therapy: absence of cardiac hypertrophy and fibrosis, Br. J. Pharmacol. 136 (2002) 685–692.

[23] O. Cazorla, S. Szilagyi, J.-Y. Le Guennec, G. Vassort, A. Lacampagne, Transmural stretch-dependent regulation of contractile properties in rat heart and its alteration after myocardial infarction, FASEB J. 19 (2005) 88–90.

[24] J. Fauconnier, A. Lacampagne, J.-M. Rauzier, G. Vassort, S. Richard, Ca^{2+}-dependent reduction of IK1 in rat ventricular cells: a novel paradigm for arrhythmia in heart failure? Cardiovasc. Res. 68 (2005) 204–212.

[25] L. Andre, J. Boissière, C. Reboul, R. Perrier, S. Zalvidea, G. Meyer, et al., Carbon monoxide pollution promotes cardiac remodeling and ventricular arrhythmia in healthy rats, Am. J. Respir. Crit. Care Med. 181 (2010) 587–595.

[26] F. Hohendanner, S. Walther, J.T. Maxwell, S. Kettlewell, S. Awad, G.L. Smith, et al., Inositol-1,4,5-trisphosphate induced Ca^{2+} release and excitation-contraction coupling in atrial myocytes from normal and failing hearts, J. Physiol. 593 (2015) 1459–1477.

[27] N. MacQuaide, J. Dempster, G.L. Smith, Assessment of sarcoplasmic reticulum Ca^{2+} depletion during spontaneous Ca^{2+} waves in isolated permeabilized rabbit ventricular cardiomyocytes, Biophys. J. 96 (2009) 2744–2754.

[28] J. Thireau, S. Zalvidea, P. Meschin, J.-L. Pasquie, F. Aimond, S. Richard, ACE inhibitor delapril prevents $Ca(2+)$-dependent blunting of IK1 and ventricular arrhythmia in ischemic heart disease, Curr. Mol. Med. 15 (2015) 642–651.

[29] N. MacQuaide, J. Dempster, G.L. Smith, Measurement and modeling of Ca^{2+} waves in isolated rabbit ventricular cardiomyocytes, Biophys. J. 93 (2007) 2581–2595.

[30] H. Kim, H.-J. Yoon, H.-S. Park, Y.-K. Cho, C.-W. Nam, S.-H. Hur, et al., Usefulness of tissue Doppler imaging-myocardial performance index in the evaluation of diastolic dysfunction and heart failure with preserved ejection fraction, Clin. Cardiol. 34 (2011) 494–499.

[31] C. Tei, L.H. Ling, D.O. Hodge, K.R. Bailey, J.K. Oh, R.J. Rodeheffer, et al., New

index of combined systolic and diastolic myocardial performance: a simple and reproducible measure of cardiac function–a study in normals and dilated cardiomyopathy, J. Cardiol. 26 (1995) 357–366.

[32] T.D. Nguyen, Y. Shingu, M. Schwarzer, A. Schrepper, T. Doenst, The E-wave deceleration rate E/DT outperforms the tissue Doppler-derived index E/e' in characterizing lung remodeling in heart failure with preserved ejection fraction, PLoS One 8 (2013) e82077.

[33] O. Cazorla, Y. Wu, T.C. Irving, H. Granzier, Titin-based modulation of calcium sensitivity of active tension in mouse skinned cardiac myocytes, Circ. Res. 88 (2001) 1028–1035.

[34] H. Cheng, W.J. Lederer, Calcium sparks, Physiol. Rev. 88 (2008) 1491–1545.

[35] J. Fauconnier, J. Thireau, S. Reiken, C. Cassan, S. Richard, S. Matecki, et al., Leaky RyR2 trigger ventricular arrhythmias in Duchenne muscular dystrophy, Proc. Natl. Acad. Sci. U. S. A. 107 (2010) 1559–1564.

[36] J. Thireau, S. Karam, S. Roberge, J. Roussel, F. Aimond, C. Cassan, et al., β-adrenergic blockade combined with subcutaneous B-type natriuretic peptide: a promising approach to reduce ventricular arrhythmia in heart failure? Heart Br. Card. Soc. 100 (2014) 833–841.

[37] M. Fernández-Velasco, A. Rueda, N. Rizzi, J.-P. Benitah, B. Colombi, C. Napolitano, et al., Increased Ca^{2+} sensitivity of the ryanodine receptor mutant RyR2R4496C underlies catecholaminergic polymorphic ventricular tachycardia, Circ. Res. 104 (2009) 201–209 (12p following 209).

[38] F. Aimond, J.L. Alvarez, J.M. Rauzier, P. Lorente, G. Vassort, Ionic basis of ventricular arrhythmias in remodeled rat heart during long-term myocardial infarction, Cardiovasc. Res. 42 (1999) 402–415.

[39] S. Kääb, H.B. Nuss, N. Chiamvimonvat, B. O'Rourke, P.H. Pak, D.A. Kass, et al., Ionic mechanism of action potential prolongation in ventricular myocytes from dogs with pacing-induced heart failure, Circ. Res. 78 (1996) 262–273.

[40] S. Richard, F. Leclercq, S. Lemaire, C. Piot, J. Nargeot, Ca^{2+} currents in compensated hypertrophy and heart failure, Cardiovasc. Res. 37 (1998) 300–311.

[41] E. Perrier, B.-G. Kerfant, N. Lalevee, P. Bideaux, M.F. Rossier, S. Richard, et al., Mineralocorticoid receptor antagonism prevents the electrical remodeling that precedes cellular hypertrophy after myocardial infarction, Circulation 110 (2004) 776–783.

[42] F.R. Heinzel, F. Hohendanner, G. Jin, S. Sedej, F. Edelmann, Myocardial hypertrophy and its role in heart failure with preserved ejection fraction, J. Appl. Physiol. (1985) 119 (2015) 1233–1242.

[43] G. Conceição, I. Heinonen, A.P. Lourenço, D.J. Duncker, I. Falcão-Pires, Animal models of heart failure with preserved ejection fraction, Neth. Hear. J. 24 (2016) 275–286.

[44] M. Klapholz, M. Maurer, A.M. Lowe, F. Messineo, J.S. Meisner, J. Mitchell, et al., Hospitalization for heart failure in the presence of a normal left ventricular ejection fraction: results of the New York Heart Failure Registry, J. Am. Coll. Cardiol. 43 (2004) 1432–1438.

[45] A.A. Oktay, S.J. Shah, Current perspectives on systemic hypertension in heart failure with preserved ejection fraction, Curr. Cardiol. Rep. 16 (2014) 545.

[46] Å.T. Røe, J.M. Aronsen, K. Skårdal, N. Hamdani, W.A. Linke, H.E. Danielsen, et al., Increased passive stiffness promotes diastolic dysfunction despite improved Ca^{2+} handling during left ventricular concentric hypertrophy, Cardiovasc. Res. (2017), https://doi.org/10.1093/cvr/cvx087.

[47] S.R. Houser, K.B. Margulies, A.M. Murphy, F.G. Spinale, G.S. Francis, S.D. Prabhu, et al., Animal models of heart failure, Circ. Res. 111 (2012) 131–150.

[48] B.M. Massie, P.E. Carson, J.J. McMurray, M. Komajda, R. McKelvie, M.R. Zile, et al., Irbesartan in patients with heart failure and preserved ejection fraction, N. Engl. J. Med. 359 (2008) 2456–2467.

[49] A.M. Shah, B. Claggett, N.K. Sweitzer, S.J. Shah, I.S. Anand, E. O'Meara, et al., Cardiac structure and function and prognosis in heart failure with preserved ejection fraction: findings from the echocardiographic study of the Treatment of Preserved Cardiac Function Heart Failure with an Aldosterone Antagonist (TOPCAT) trial, Circ Heart Fail. 7 (2014) 740–751.

[50] L. van Heerebeek, A. Borbély, H.W.M. Niessen, J.G.F. Bronzwaer, J. van der Velden, G.J.M. Stienen, et al., Myocardial structure and function differ in systolic and diastolic heart failure, Circulation 113 (2006) 1966–1973.

[51] L. van Heerebeek, N. Hamdani, M.L. Handoko, I. Falcao-Pires, R.J. Musters, K. Kupreishvili, et al., Diastolic stiffness of the failing diabetic heart: importance of fibrosis, advanced glycation end products, and myocyte resting tension, Circulation 117 (2008) 43–51.

[52] W.J. Paulus, C. Tschöpe, A novel paradigm for heart failure with preserved ejection fraction: comorbidities drive myocardial dysfunction and remodeling through coronary microvascular endothelial inflammation, J. Am. Coll. Cardiol. 62 (2013) 263–271.

[53] C. Tschöpe, S. Van Linthout, New insights in (inter)cellular mechanisms by heart failure with preserved ejection fraction, Curr. Heart Fail. Rep. 11 (2014) 436–444.

[54] D.J. Beuckelmann, M. Näbauer, E. Erdmann, Intracellular calcium handling in isolated ventricular myocytes from patients with terminal heart failure, Circulation 85 (1992) 1046–1055.

[55] R. Coronel, R. Wilders, A.O. Verkerk, R.F. Wiegerinck, D. Benoist, O. Bernus, Electrophysiological changes in heart failure and their implications for arrhythmogenesis, Biochim. Biophys. Acta 2013 (1832) 2432–2441.

[56] M. Lindner, M.C. Brandt, H. Sauer, J. Hescheler, T. Böhle, D.J. Beuckelmann, Calcium sparks in human ventricular cardiomyocytes from patients with terminal heart failure, Cell Calcium 31 (2002) 175–182.

[57] M. Luo, M.E. Anderson, Ca^{2+} cycling in heart failure, Circ. Res. 113 (2013) 690–708.

[58] S.O. Marx, A.R. Marks, Dysfunctional ryanodine receptors in the heart: new insights into complex cardiovascular diseases, J. Mol. Cell. Cardiol. 58 (2013) 225–231.

[59] M. Methawasin, J.G. Strom, R.E. Slater, V. Fernandez, C. Saripalli, H. Granzier, Experimentally increasing the compliance of titin through RNA binding motif-20 (RBM20) inhibition improves diastolic function in a mouse model of heart failure with preserved ejection fraction, Circulation 134 (2016) 1085–1099.

[60] U. Primessnig, P. Schönleitner, A. Höll, S. Pfeiffer, T. Bracic, T. Rau, et al., Novel pathomechanisms of cardiomyocyte dysfunction in a model of heart failure with preserved ejection fraction, Eur. J. Heart Fail. 18 (2016) 987–997.

[61] B.M.R. Carvalho, R.A. Bassani, K.G. Franchini, J.W.M. Bassani, Enhanced calcium mobilization in rat ventricular myocytes during the onset of pressure overload-induced hypertrophy, Am. J. Physiol. Heart Circ. Physiol. 291 (2006) H1803–H1813.

[62] D.A. Eisner, A.W. Trafford, M.E. Díaz, C.L. Overend, S.C. O'Neill, The control of Ca release from the cardiac sarcoplasmic reticulum: regulation versus autoregulation, Cardiovasc. Res. 38 (1998) 589–604.

[63] L.A. Venetucci, A.W. Trafford, S.C. O'Neill, D.A. Eisner, Na/Ca exchange: regulator of intracellular calcium and source of arrhythmias in the heart, Ann. N. Y. Acad. Sci. 1099 (2007) 315–325.

[64] B.C. Willis, S.V. Pandit, D. Ponce-Balbuena, M. Zarzoso, G. Guerrero-Serna, B. Limbu, et al., Constitutive intracellular Na^{+} 4, Circulation 133 (2016) 2348–2359.

[65] K.E. Runte, S.P. Bell, D.E. Selby, T.N. Häußler, T. Ashikaga, M.M. LeWinter, et al., Relaxation and the role of calcium in isolated contracting myocardium from patients with hypertensive heart disease and heart failure with preserved ejection fraction, Circ Heart Fail. 10 (2017), https://doi.org/10.1161/CIRCHEARTFAILURE.117.004311.

[66] E.D. Fowler, C.H.T. Kong, J.C. Hancox, M.B. Cannell, Late Ca^{2+}Sparks and ripples during the systolic Ca2 + transient in heart muscle cells, Circ. Res. 122 (2018) 473–478.

[67] A. Mattiazzi, E.G. Kranias, The role of CaMKII regulation of phospholamban activity in heart disease, Front. Pharmacol. 5 (2014) 5.

[68] G. Chu, E.G. Kranias, Functional interplay between dual site phospholambam phosphorylation: insights from genetically altered mouse models, Basic Res. Cardiol. 97 (Suppl. 1) (2002) I43–I48.

[69] A.G. Brittsan, K.S. Ginsburg, G. Chu, A. Yatani, B.M. Wolska, A.G. Schmidt, et al., Chronic SR Ca^{2+}-ATPase inhibition causes adaptive changes in cellular Ca^{2+} transport, Circ. Res. 92 (2003) 769–776.

[70] A. Mattiazzi, C. Mundiña-Weilenmann, C. Guoxiang, L. Vittone, E. Kranias, Role of phospholamban phosphorylation on Thr17 in cardiac physiological and pathological conditions, Cardiovasc. Res. 68 (2005) 366–375.

[71] G.D. Mills, H. Kubo, D.M. Harris, R.M. Berretta, V. Piacentino, S.R. Houser, Phosphorylation of phospholamban at threonine-17 reduces cardiac adrenergic contractile responsiveness in chronic pressure overload-induced hypertrophy, Am. J. Physiol. Heart Circ. Physiol. 291 (2006) H61–H70.

[72] D. Hagemann, R.-P. Xiao, Dual site phospholamban phosphorylation and its physiological relevance in the heart, Trends Cardiovasc. Med. 12 (2002) 51–56.

[73] A.R. Marks, Calcium cycling proteins and heart failure: mechanisms and therapeutics, J. Clin. Invest. 123 (2013) 46–52.

[74] X. Ai, J.W. Curran, T.R. Shannon, D.M. Bers, S.M. Pogwizd, Ca^{2+}/calmodulin-dependent protein kinase modulates cardiac ryanodine receptor phosphorylation and sarcoplasmic reticulum Ca^{2+} leak in heart failure, Circ. Res. 97 (2005) 1314–1322.

[75] D. Eisner, Calcium in the heart: from physiology to disease, Exp. Physiol. 99 (2014) 1273–1282.

[76] D.A. Eisner, T. Kashimura, S.C. O'Neill, L.A. Venetucci, A.W. Trafford, What role does modulation of the ryanodine receptor play in cardiac inotropy and arrhythmogenesis? J. Mol. Cell. Cardiol. 46 (2009) 474–481.

[77] S.A. Goonasekera, J.D. Molkentin, Unraveling the secrets of a double life: Contractile versus signaling Ca^{2+} in a cardiac myocyte, J. Mol. Cell. Cardiol. 52 (2012) 317–322.

[78] S. Horgan, C. Watson, N. Glezeva, J. Baugh, Murine models of diastolic dysfunction and heart failure with preserved ejection fraction, J. Card. Fail. 20 (2014) 984–995.

[79] G. Tarone, J.-L. Balligand, J. Bauersachs, A. Clerk, L. De Windt, S. Heymans, et al., Targeting myocardial remodelling to develop novel therapies for heart failure: a position paper from the working group on myocardial function of the European Society of Cardiology, Eur. J. Heart Fail. 16 (2014) 494–508.

[80] M. Schnelle, N. Catibog, M. Zhang, A.A. Nabeebaccus, G. Anderson, D.A. Richards, et al., Echocardiographic evaluation of diastolic function in mouse models of heart disease, J. Mol. Cell. Cardiol. 114 (2018) 20–28.

[81] G. Güder, J. Bauersachs, S. Frantz, D. Weismann, B. Allolio, G. Ertl, et al., Complementary and incremental mortality risk prediction by cortisol and aldosterone in chronic heart failure, Circulation 115 (2007) 1754–1761.

[82] D.W. Kitzman, W.C. Little, P.H. Brubaker, R.T. Anderson, W.G. Hundley, C.T. Marburger, et al., Pathophysiological characterization of isolated diastolic heart failure in comparison to systolic heart failure, JAMA 288 (2002) 2144–2150.

[83] K.M. Baker, M.I. Chernin, S.K. Wixson, J.F. Aceto, Renin-angiotensin system involvement in pressure-overload cardiac hypertrophy in rats, Am. J. Phys. 259 (1990) H324–H332.

[84] R. Mohabir, S.D. Young, A.M. Strosberg, Role of angiotensin in pressure overload-induced hypertrophy in rats: effects of angiotensin-converting enzyme inhibitors, an AT1 receptor antagonist, and surgical reversal, J. Cardiovasc. Pharmacol. 23 (1994) 291–299.